Analytical computation of neutron recoil spectra for rare-event backgrounds

A.J. Biffl[1,*] and A.N. Villano[1,†]

[1] Department of Physics, University of Colorado Denver, Denver, Colorado 80217, USA

(Dated: July 11, 2024)

We calculate the neutron-induced recoil spectrum in homogenous material for a known isotropic neutron flux without Monte Carlo techniques. The goal of our approach is to provide an alternative and complementary method for computing background spectra in rare-event searches. Typically, Monte Carlo techniques require detailed geometry constructions and in low-rate environments will yield very few counts in the signal region for hundreds of years of exposure–which may be computationally intensive. Our method removes this counting uncertainty in favor of uncertainty in the initial flux, which can be assessed by multiple means.

I. INTRODUCTION

In almost all modern experiments, computation of interaction rates and spectra in particle detectors uses Monte Carlo (MC) methods (e.g., [1–7]). However, for rare events, when the expected signal size is many orders of magnitude smaller than the primary sample size, MC methods can be extremely expensive [8], and even so-called variance reduction schemes such as importance biasing [9] and forward flux sampling [10] may not substantially reduce the cost of these computations [11, 12]. This paper presents a partial alternative to MC simulations, a method for calculating neutron-induced recoil spectra in silicon detectors that does not use any MC techniques.

Most particle detector simulations can be broken up into two parts: particle propagation and detector response. For the case of estimating neutron-induced signals, these correspond to estimation of the neutron flux spectrum and estimation of the neutron-induced recoil spectrum (and, in some cases, modeling of further processes in the detector such as charge or phonon transportation, but these are ignored here). This paper presents the second of these parts, an analytical procedure to take an incident neutron flux spectrum as input and output the expected neutron-induced recoil distribution in silicon detectors. An input neutron flux spectrum is described in section II. The "single scatter" spectrum is described in section III, which assumes the neutron flux is uniform in the detector volume and that neutrons will interact only once. Multiple scatters, from neutrons which interact more than once, are treated in section IV. The resulting recoil spectrum is compared to MC simulation in section V, and concluding remarks are given in section VI.

* Corresponding author: alexander.biffl@ucdenver.edu

† Corresponding author: anthony.villano@ucdenver.edu

II. FLUX

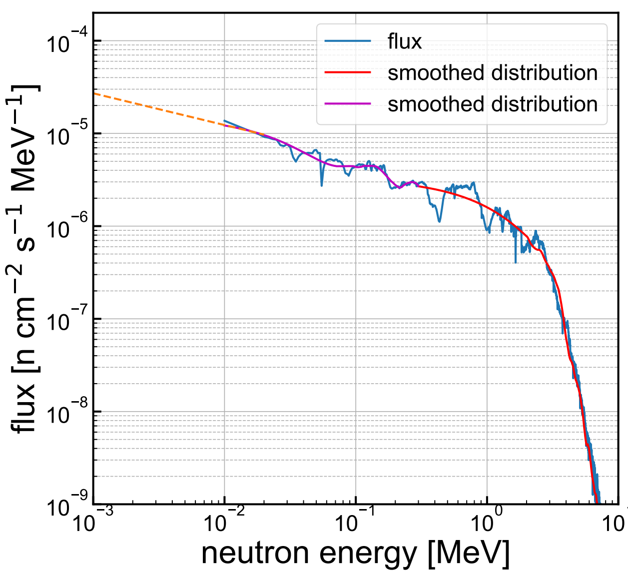

FIG. 1. (Color online) Estimated neutron flux in the SNOLAB environment above 1 keV neutron energy. The high-energy flux (blue) is derived from the simulated neutron flux of the Super Cryogenic Dark Matter Search (SuperCDMS) for the SNOLAB environment [13]. The red and purple curves are smoothings of the same. The yellow dashed curve is an extrapolation down to 1 keV based on a linear model.

III. SINGLE SCATTERS

Given an incident neutron flux spectrum, the rate of interactions with detector materials follows from first principles. The number of recoils with energy E_r per unit time per unit energy in the detector $N(E_r)$ is:

$$N(E_r) = n \int_0^\infty \int_V \phi(E_n, \boldsymbol{x}) \frac{d\sigma(E_r, E_n)}{dE_r} d\boldsymbol{x} dE_n \tag{1}$$

where $\phi(E_n, \boldsymbol{x})$ is the flux density of neutrons (neutrons per unit area per unit time per unit energy) at neutron energy E_n and position $\boldsymbol{x}$, and $d\sigma/dE_r$ is the differential scattering cross section for recoil energy E_r.

A useful parameterization of the spectrum is the DRU rate of scatters per unit detector mass $R(E_r)$:

$$R(E_r) = \frac{N(E_r)}{nVm_{Si}} \tag{2}$$

In a 1 cm × 1 cm × 4 mm silicon detector, the spatial dependence of the flux was estimated using the diffusion approximation in the absence of external sources or in-scattering (see Appendix A). The rate was only reduced by 0.20% from uniform in the center of the detector, and the average flux over the whole detector was only reduced by 0.083%. Thus, the flux was approximated as uniform to simplify calculations. Then the spatial integral in (1) evaluates to V, the detector volume, and we arrive at an approximation for the rate of "first" scatters, scatters with neutrons that have not interacted in the detector yet:

$$R(E_r) = \frac{1}{m_{Si}} \int_0^\infty \phi(E_n) \frac{d\sigma(E_r, E_n)}{dE_r} dE_n \tag{3}$$

Evaluated cross section data was taken from the ENDF/B-VIII database [14], which gives tabulated values and interpolation laws for the cross sections $\sigma(E_n)$, as well as the distributions of scattering-angle cosine μ, $f(\mu, E_n)$. Since $E_r = \alpha E_n(1-\mu)$ (where $\alpha = 2A/(A+1)^2$ for mass number A), the differential cross sections can be calculated as:

$$\frac{d\sigma(E_r, E_n)}{dE_r} = \frac{\sigma(E_n)}{2\pi\alpha E_n} f(1 - E_r/\alpha E_n, E_n) \tag{4}$$

The integral (3) can be evaluated numerically with trapezoidal integration to high accuracy. The resulting recoil spectrum is plotted in Figure 2. Cumulative numerical errors associated with the choice of energy grid in the integral were found to be on the order of 10^{-4}%. Errors associated with the evaluation of the differential cross sections were found to be of the same magnitude.

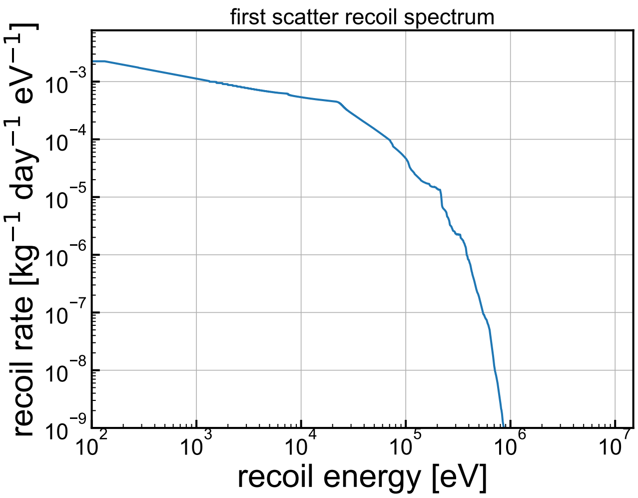

FIG. 2. (Color online) Spectrum of first scatters $R(E_r)$

IV. MULTIPLE SCATTERS

In general it is possible that a neutron will scatter multiple times in the detector. To estimate the rate at which this happens, we assume isotropic scattering and (as in the previous section) homogeneous flux (see Appendix B). Then, the counting rate of ith scatters (scatters of neutrons that have already interacted $i-1$ times) is:

$$N_i(E_r) = nV \int_0^\infty \phi_i(E_n) \frac{d\sigma(E_r, E_n)}{dE_r} dE_n \tag{5}$$

with the ith flux $\phi_i(E_n)$ defined by:

$$\phi_i(E_n) \equiv n\ell \int_{E_n}^\infty \phi_{i-1}(E_n') \frac{d\sigma(E_n' - E_n, E_n')}{dE_r} dE_n' \tag{6}$$

where $\phi_1(E_n)$ is the external incident flux and ℓ is a characteristic length of the detector, calculated by a double integral over the detector volume:

$$\ell \equiv \frac{1}{V} \iint \frac{1}{4\pi|\boldsymbol{x} - \boldsymbol{x'}|^2} d\boldsymbol{x'} d\boldsymbol{x} \tag{7}$$

For a 1 cm × 1 cm × 4 mm detector, the characteristic length ℓ is approximately 0.307784 cm. The resulting first three ith fluxes are plotted in Figure 3, and the first three scatter spectra are plotted in Figure 9 in Appendix B. The total scatter rates, and their percentage of the first-scatter rate, are given in Table I. Beyond $i = 6$, the effects become smaller than one part in 4×10^6 and are neglected.

i	rate (kg^{-1} day^{-1})	percent of first scatters
1	27.918	100.0000%
2	1.729	6.1929%
3	0.13079	0.4685%
4	0.01113	0.0399%
5	0.00098173	0.0035%
6	8.4606e-05	0.0003%
total	29.79	106.7051%

TABLE I. Total rate of ith scatters up to $i = 6$.

A. Summing energy deposits

In essentially every type of semiconductor-based detector, the scattering events caused by a single neutron will not be able to be distinguished from each other. For

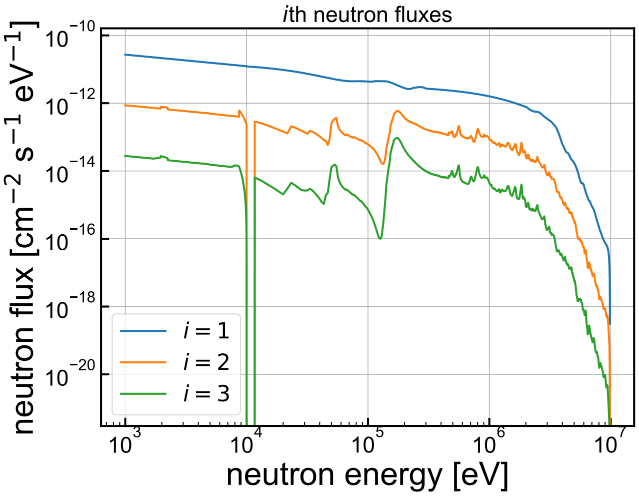

FIG. 3. (Color online) ith fluxes $\phi_i(E_n)$ up to $i = 3$. Higher-i fluxes continue the pattern of being suppressed by a factor of $\sim$30, and the pattern of peaks and troughs mirroring the cross section are further amplified.

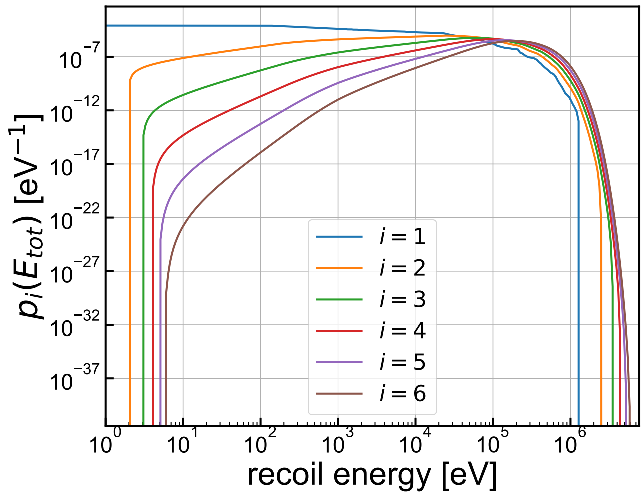

FIG. 4. (Color online) Sum probabilities $p_i(E_{tot})$ up to $i = 6$. Note the fall to zero below a few eV is nonphysical, and is a result of the finite energy grid truncating at 1 eV.

phonon propagation speeds $\lesssim 10^4$ m/s, a variation in path lengths from phonon emission site to detector terminal of 0.5 mm (c.f., 0.65 mm impact-disturbed charge cloud radius fit by [15]) causes a minimum width of the signal peak of $\gtrsim$50 ns. For charge propagation speeds of $\sim 10^5$ m/s with the same variation in path lengths, there is a minimum signal peak width of $\sim$ 5 ns. On the other hand, a 1 MeV neutron only takes 0.7 ns to travel across a cm-wide detector, making distinguishing the peaks from two consecutive scatters effectively impossible (no matter how detector technologies improve from current $\sim \mu$s resolutions). Each series of scatters will seem to contribute to a single event in the detector, with energy equal to the sum of deposits from each of the individual scatters. We are thus interested in the probability $p_i(E_{tot})$ of total energy $E_{tot} = \sum_{j=1}^{i} E_{r,j}$ deposited in i scatters:

$$p_i(E_{tot}) = \int_0^{E_{tot}} p_{i-1}(E_{tot} - E_r)\dot{p}^{RR}(E_r|E_{tot} - E_r)dE_r \tag{8}$$

with the notation $\dot{p}^{RR}(E'_r|E_r)$ denoting the probability of a scatter with energy E'_r, given E_r was deposited in the previous scatters (see Appendix C). The $p_i(E_{tot})$ up to $i = 6$ are plotted in Figure 4

To then calculate the overall resulting spectrum, define the total rate of ith scatters $\boldsymbol{R}_i \equiv \int R_i(E_r)dE_r$, and the rate of scatters where the neutron scatters *exactly* i times $\rho_i = \boldsymbol{R}_i - \boldsymbol{R}_{i+1}$. Then the net spectrum of counts in the detector is $\sum_i \rho_i p_i(E_r)$. This is plotted in Figure 5 alongside the single scatter spectrum $\rho_1 p_1(E_r)$.

V. COMPARISON WITH MONTE CARLO

The example calculation given above was compared to a traditional MC calculation by simulating neutrons hitting a 1 cm × 1 cm × 4 mm block of silicon in `SuperSim`, a simulations framework built on top of Geant4 by the SuperCDMS collaboration [5]. 10^8 neutrons were thrown from the surface of the block of silicon, distributed according to the spectrum presented in Section II. Neutron trajectories were distributed as a Lambertian (proportional to the cosine of the angle with the surface normal) to mimic an isotropic flux at the surface [16]. The resulting spectra of induced recoils from single- and multiple-scattering neutrons, normalized to the integral of the flux presented in section II, is plotted in the top panel of Figure 6 alongside the final spectra of singles, $\rho_1 p_1(E_r)$, and multiples, $\sum_{i=2}^{6} \rho_i p_i(E_r)$, calculated in the previous section. The bottom panel shows the relative error between each spectrum and its corresponding simulation.

The simulated spectrum agrees extremely well with

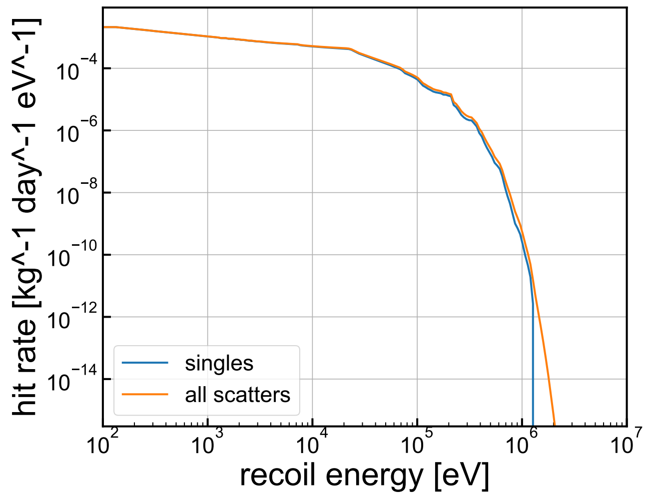

FIG. 5. (Color online) Spectrum of all scatters $\sum_i \rho_i p_i(E_r)$ plotted alongside $\rho_1 p_1(E_r)$, the spectrum of neutrons that scatter exactly once.

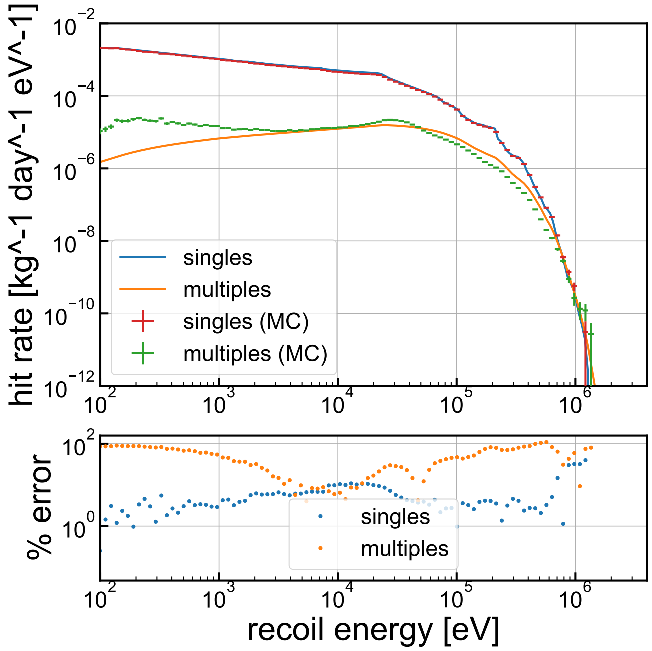

FIG. 6. (Color online) Comparison of simulation results with predictions from Figure 5, split into single- and multiple- scattering neutrons. (top): DRU spectra (bottom): error between predictions and simulation, relative to simulated spectrum.

our predictions, particularly for single-scattering neutrons. Systematic errors on the order of 10% peaking at 10 keV are most likely explained by self-shielding effects (though the deviation is about two orders of magnitude larger than our predictions for the suppression in rate due to self-shielding, see Appendix A). Larger errors in the spectrum of multiply-scattering neutrons are caused by two main phenomena. First, self-shielding is amplified in later scatters. Second, angular correlations become more important in multiple scatters – a neutron that has already interacted more than once is more likely to be travelling away from the center of the detector, decreasing its ability to cause higher-i scatters, contrary to the isotropic-emission treatment outlined in Appendix B.

VI. CONCLUSION

ACKNOWLEDGMENTS

Appendix A: Spatial Dependence of the First Flux

To evaluate the spatial dependence of the first flux (the flux of neutrons that haven't scattered yet), the steady-state neutron diffusion equation was applied, assuming isotropic scattering and the absence of external sources or in-scattering (External sources are neglected because most detectors are likely made from high-purity materials with minimal radioactivity. In-scattering is neglected from here as we are only interested in the first flux). Then, at all energies the flux obeys the condition:

$$\nabla^2\phi = 3\Sigma_t^2\phi \tag{A1}$$

where $\Sigma_t(E) = n\sigma(E)$ is the total scattering macroscopic cross section. In a rectangular detector with dimensions $L_x \times L_y \times L_z$ centered at the origin, and uniform flux $\phi_1(E)$ on the surface, the flux is:

$$\phi(x,y,z) = \phi_x(x,y,z) + \phi_y(x,y,z) + \phi_z(x,y,z) \tag{A2a}$$

$$\phi_x(x,y,z) = \sum_{m\text{ odd}}\sum_{n\text{ odd}} \frac{16\phi_1(E)}{\pi^2 mn}\frac{\cosh(\rho^x_{mn}x)}{\cosh(\rho^x_{mn}L_x/2)} \times \sin\left(\frac{n\pi}{L_z}(z+L_z/2)\right)\sin\left(\frac{m\pi}{L_y}(y+L_y/2)\right) \tag{A2b}$$

$$\phi_y(x,y,z) = \sum_{m\text{ odd}}\sum_{n\text{ odd}} \frac{16\phi_1(E)}{\pi^2 mn}\frac{\cosh(\rho^y_{mn}y)}{\cosh(\rho^y_{mn}L_y/2)} \times \sin\left(\frac{n\pi}{L_x}(x+L_x/2)\right)\sin\left(\frac{m\pi}{L_z}(z+L_z/2)\right) \tag{A2c}$$

$$\phi_z(x,y,z) = \sum_{m\text{ odd}}\sum_{n\text{ odd}} \frac{16\phi_1(E)}{\pi^2 mn}\frac{\cosh(\rho^z_{mn}z)}{\cosh(\rho^z_{mn}L_z/2)} \times \sin\left(\frac{n\pi}{L_x}(x+L_x/2)\right)\sin\left(\frac{m\pi}{L_y}(y+L_y/2)\right) \tag{A2d}$$

where

$$\rho^x_{mn} = \sqrt{3\Sigma_t^2 + \frac{n^2\pi^2}{L_z^2} + \frac{m^2\pi^2}{L_y^2}} \tag{A3a}$$

$$\rho^y_{mn} = \sqrt{3\Sigma_t^2 + \frac{n^2\pi^2}{L_x^2} + \frac{m^2\pi^2}{L_z^2}} \tag{A3b}$$

$$\rho^z_{mn} = \sqrt{3\Sigma_t^2 + \frac{n^2\pi^2}{L_x^2} + \frac{m^2\pi^2}{L_y^2}} \tag{A3c}$$

Integrating over the volume of the detector, the effective flux ratio $Q(E) \equiv (\int_V \phi(E) d^3\boldsymbol{x})/(V\phi_1(E))$ is:

$$Q(E) = Q_x(E) + Q_y(E) + Q_z(E) \tag{A4a}$$

$$Q_z(E) = \frac{128}{\pi^4 L_z}\sum_{m\text{ odd}}\sum_{n\text{ odd}}\frac{\tanh(\rho^z_{mn}L_z/2)}{m^2n^2\rho^z_{mn}} \tag{A4b}$$

and similarly for Q_x and Q_y.

This was estimated numerically with n and m going up to 1,001. The resulting effective flux *reduction* $1 - Q(E)$ is plotted alongside the macroscopic cross section $\Sigma_t(E)$ in Figure 7. The flux reduction exactly parallels the cross section (it actually more closely matches Σ_t^2, although the two large resonance troughs at 53.3 keV and 144.9 keV are less deep in the flux reduction data).

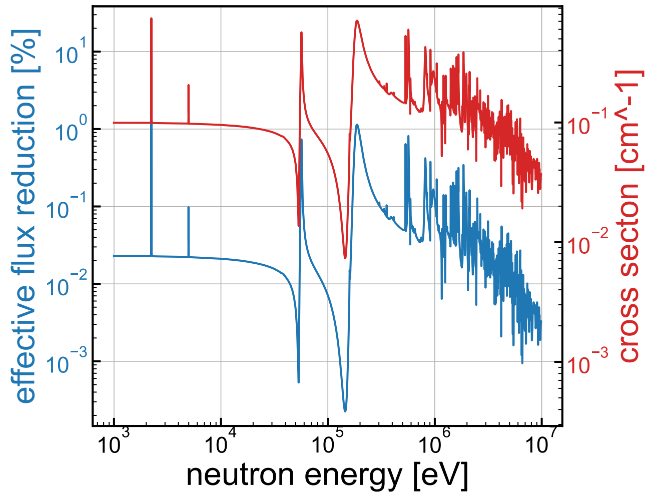

FIG. 7. (Color online) Effective flux reduction $1-Q(E)$ (blue, left axes) and macroscopic cross section for elastic scatters in silicon $\Sigma_t(E)$ (red, right axes)

The exact interaction rate (1) can be calculated as:

$$N(E_r) = nV \int_0^\infty Q(E_n)\phi_1(E_n)\frac{d\sigma(E_r, E_n)}{dE_r}dE_n \quad \text{(A5)}$$

The resulting rate reduction is plotted in Figure 8.

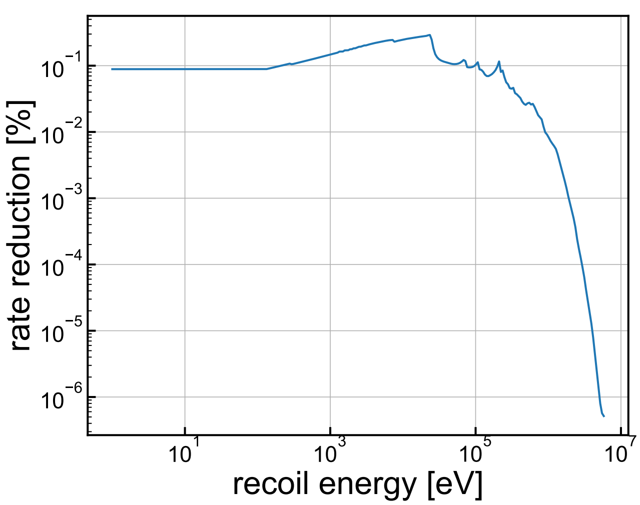

FIG. 8. (Color online) Relative reduction in total interaction spectrum $\sum_i \rho_i p_i(E_r)$

Appendix B: Derivation of multiple-scatter rates

One can approximate a nucleus that has been collided with as an isotropic source of neutrons, with emission rate given by the rate at which neutrons "leave" a first-scatter with the given energy:

$$dR'(E'_n) = \int_{E'_n}^\infty \phi(E_n)\frac{d\sigma(E_n - E'_n, E_n)}{dE_r}dE_n \quad \text{(B1)}$$

where we've parameterized by the post-collision neutron energy $E'_n = E_n - E_r$.

The flux of neutrons $i(E'_n)$ some distance ϱ from that nucleus is then:

$$i(E'_n) = \frac{dR'(E'_n)}{4\pi\varrho^2} \quad \text{(B2)}$$

The total once-collided flux $\phi'(E'_n, \boldsymbol{x})$ at a position $\boldsymbol{x}$ is then $i(E'_n)$ integrated over all nuclei in the detector:

$$\phi'(E'_n, \boldsymbol{x}) = n\int_V \frac{dR'(E'_n)}{4\pi(\boldsymbol{x}-\boldsymbol{x'})^2}d\boldsymbol{x'} \quad \text{(B3)}$$

The rate of second scatters in the detector is then:

$$N_2(E'_r) = n\int_0^\infty \int_V \phi'(E'_n, \boldsymbol{x})\frac{d\sigma(E'_r, E'_n)}{dE_r}d\boldsymbol{x}dE'_n \quad \text{(B4)}$$

Expanding this out and using the characteristic length ℓ defined in (7) results in the expression:

$$N_2(E_r) = n^2\ell V \int_0^\infty dR'(E'_n)\frac{d\sigma(E'_r, E'_n)}{dE_r}dE'_n \quad \text{(B5)}$$

If we now define the "second flux" of neutrons $\phi_2(E'_n)$

$$\phi_2(E'_n) \equiv n\ell dR'(E'_n) = n\ell\int_{E'_n}^\infty \phi(E_n)\frac{d\sigma(E_n - E'_n, E_n)}{dE_r}dE_n \quad \text{(B6)}$$

we get

$$N_2(E'_r) = nV\int_0^\infty \phi_2(E'_n)\frac{d\sigma(E'_r, E'_n)}{dE_r}dE'_n \quad \text{(B7)}$$

which is exactly analogous to (3). The relations for the general ith rates and fluxes, (5) and (6), follow by analogy from these.

For a 1 cm × 1 cm × 4 mm detector, the characteristic length ℓ is approximately 0.307784 cm. The resulting first three ith fluxes are plotted in Figure 3, and the first three scatter spectra are plotted in Figure 9.

Appendix C: Summing energy deposits

In Section IV A, we noted that we are interested in the distribution of the total energy deposited by a neutron between multiple scatters:

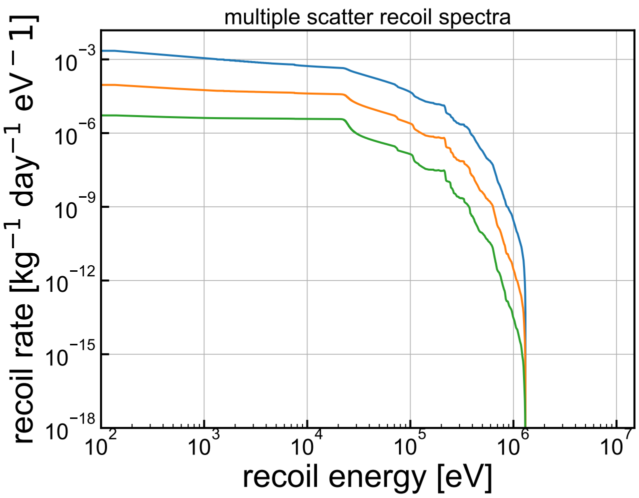

FIG. 9. (Color online) ith recoil spectra $R_i(E_r)$ up to $i = 3$

$$p_i(E_{tot}) = \int_0^{E_{tot}} p_{i-1}(E_{tot} - E_r)\dot{p}^{RR}(E_r|E_{tot} - E_r)dE_r \tag{C1}$$

$\dot{p}^{RR}(E'_r|E_r)$ is the probability of a scatter with energy E'_r given E_r was deposited in the previous scatters. Marginalizing on the neutron's energy right before the last scatter, E_n:

$$\dot{p}^{RR}(E'_r|E_r) = \int_0^{\infty} \tilde{p}^{RN}(E'_r|E_n)\hat{p}^{NR}(E_n|E_r)dE_n \tag{C2}$$

with $\tilde{p}^{RN}(E'_r|E_n)$ the probability the neutron causes an E'_r recoil given it had energy E_n. This is proportional to the differential cross section:

$$\tilde{p}^{RN}(E'_r|E_n) = \frac{1}{\sigma(E_n)}\frac{d\sigma(E'_r, E_n)}{dE_r} \tag{C3}$$

$\hat{p}^{NR}(E_n|E_r)$ is the probability the neutron has an energy E_n after it has deposited a total energy of E_r. This is just proportional to the incident flux at energy E_n+E_r:

$$\hat{p}^{NR}(E_n|E_r) = \frac{\phi_1(E_r + E_n)}{\int \phi_1(E)dE} \tag{C4}$$

That is, the set of neutrons with energy E_n after depositing some fixed energy E_r is the same as the set of neutrons that initially had total energy $E_n + E_r$.

It was found the sum probabilities $p_i(E_{tot})$ could be calculated up to $i = 6$ with minimal numerical error with $\dot{p}^{RR}$ stored on a 300×300 grid of energy points between 1 eV and 20 MeV. Note that $p_1(E_r)$ was defined as $p_1(E_r) \equiv R_1(E_r)/\boldsymbol{R}_1$. The integrals were evaluated on 7,500 points with trapezoidal integration, using linear interpolation to evaluate $p_i(E_{tot})$, $\dot{p}^{RR}$, and $\hat{p}^{NR}$. It was found necessary to normalize the rows of $\dot{p}^{RR}$ manually.

Appendix D: Full treatment of spatial dependence

1. Isotropic emission

If we once again assume post-scatter neutrons are emitted isotropically in space, the rate of first scatters $f_1(E_r, \boldsymbol{x})$ per unit volume at energy E_r and position $\boldsymbol{x}$ is:

$$f_1(E_r, \boldsymbol{x}) = n\int_0^{\infty} \phi(E_n, \boldsymbol{x})\frac{d\sigma(E_r, E_n)}{dE_r}dE_n \tag{D1}$$

The corresponding emission rate of second-neutrons $e_2(E'_n, \boldsymbol{x})$ at position $\boldsymbol{x}$ and energy E'_n is:

$$e_2(E'_n, \boldsymbol{x}) = n\int_{E'_n}^{\infty} \phi_1(E_n, \boldsymbol{x})\frac{d\sigma(E_n - E'_n, E_n)}{dE_r}dE_n \tag{D2}$$

The flux of second neutrons $d\phi_2(E'_n, \boldsymbol{x}', \boldsymbol{x})$ at position $\boldsymbol{x}'$ due to $e_2(E'_n, \boldsymbol{x})$ is

$$d\phi_2(E'_n, \boldsymbol{x}', \boldsymbol{x}) = \frac{e_2(E'_n, \boldsymbol{x})}{4\pi|\boldsymbol{x} - \boldsymbol{x}'|^2} \tag{D3}$$

The total second flux $\phi_2(E_n, \boldsymbol{x}')$ is then $d\phi_2(E'_n, \boldsymbol{x}', \boldsymbol{x})$ integrated over all sources:

$$\phi_2(E_n, \boldsymbol{x}') = \int_V \frac{e_2(E'_n, \boldsymbol{x})}{4\pi|\boldsymbol{x} - \boldsymbol{x}'|^2}d\boldsymbol{x} \tag{D4}$$

and the second scatter rate $f_2(E'_r, \boldsymbol{x}')$ at position $\boldsymbol{x}'$ is:

$$f_2(E'_r, \boldsymbol{x}') = n\int_0^{\infty} \phi_2(E'_n, \boldsymbol{x}')\frac{d\sigma(E'_r, E'_n)}{dE_r}dE'_n \tag{D5}$$

In general, for the rate of ith scatters:

$$f_i(E'_r, \boldsymbol{x}') = n\int_0^{\infty} \phi_i(E'_n, \boldsymbol{x}')\frac{d\sigma(E'_r, E'_n)}{dE_r}dE'_n \tag{D6}$$

$$\phi_i(E'_n, \boldsymbol{x}') = \int_V \frac{e_i(E'_n, \boldsymbol{x})}{4\pi|\boldsymbol{x} - \boldsymbol{x}'|^2}d\boldsymbol{x} \tag{D7}$$

$$e_i(E'_n, \boldsymbol{x}) = n\int_{E'_n}^{\infty} \phi_{i-1}(E_n, \boldsymbol{x})\frac{d\sigma(E_n - E'_n, E_n)}{dE_r}dE_n \tag{D8}$$

with $\phi_1(E_n, \boldsymbol{x})$ given in the previous appendix.

The spatial dependence here can all be wrapped up into the spatially-averaged flux of i neutrons, $\bar{\phi}_i(E'_n)$:

$$\bar{\phi}_i(E'_n) \equiv \frac{1}{V}\int_V d\boldsymbol{x}'\phi_i(E'_n, \boldsymbol{x}') \tag{D9a}$$

$$= \frac{n}{V}\int_{E'_n}^{\infty} dE_n\frac{d\sigma(E_n - E'_n, E_n)}{dE_r}\iint_V d\boldsymbol{x}'d\boldsymbol{x}\frac{\phi_{i-1}(E_n, \boldsymbol{x})}{4\pi|\boldsymbol{x} - \boldsymbol{x}'|^2} \tag{D9b}$$

Then the DRU rate is:

$$R_i(E_r') = \frac{1}{m_{Si}} \int_0^\infty \bar{\phi}_i(E_n') \frac{d\sigma(E_r', E_n')}{dE_r} dE_n' \tag{D10}$$

This treatment, even ignoring angular variation in emission of $i \geq 2$ neutrons, should account for the majority of self-shielding effects, wherein the interaction rate in energy ranges with a higher cross section is suppressed more and more with growing i due to higher removal of those neutrons from the system via interaction. However, note that integrals like $\iint_V \frac{d\boldsymbol{x} d\boldsymbol{x}'}{|\boldsymbol{x}-\boldsymbol{x}'|^2}$ are extremely stiff and converge slowly, owing to the extreme peaks when $\boldsymbol{x}$ and $\boldsymbol{x}'$ are close together. In the case of (D10), these difficulties are coupled with the need to evaluate the previous flux $\phi_{i-1}(E_n, \boldsymbol{x})$ at all points $\boldsymbol{x}$ needed in the integral, making calculating (D10) extremely costly.

Note that our treatment in section IV A would also have to be revisited, as it also does not account for spatial variation in flux.

2. Including angular correlations

In an exact treatment including angular correlations, we must move from the scalar neutron flux $\phi(E, \boldsymbol{x})$ to the angular flux $\psi(E, \boldsymbol{x}, \hat{\Omega})$, giving the flux of neutrons per unit solid angle traveling in the direction of the unit vector $\hat{\Omega}$. Note that $\phi = \int_{4\pi} \psi(\hat{\Omega}) d\Omega$.

Given some initial neutron energy E_0 and some final energy E' (with recoil energy $E_r \equiv E_0 - E'$), the outgoing flux is restricted to a cone focused at $\boldsymbol{x}_0$, oriented parallel to $\hat{\Omega}_0$, with half-angle θ where $\cos\theta = 1 - E_r/\alpha E_0$. The resulting flux at a distance r along the cone is

$$\frac{n\psi \frac{d\sigma}{dE_r}}{4\pi r^2} \tag{D11}$$

Note that explicit dependence on θ cancels out, all variation being included in the factor $d\sigma/dE_r$. The change in the "area" around the cone's base with varying θ ($2\pi r^2 \sin\theta d\theta$) is exactly cancelled by the thickness of the interval $d\theta = \frac{dE_r}{\alpha E_0 \sin\theta}$ for a fixed interval dE_r.

The flux at a location $\boldsymbol{x}'$ due to interactions at $\boldsymbol{x}_0 = \boldsymbol{x}' - \lambda\hat{\Omega}'$ ($\lambda \geq 0$) is:

$$\frac{n}{4\pi\lambda^2} \int_{\mathcal{U}} d\Omega_0 \psi(E_0, \boldsymbol{x}_0, \hat{\Omega}_0) \frac{d\sigma(E_r, E_0)}{dE_r} \tag{D12}$$

where $\mathcal{U} = \mathcal{U}(\hat{\Omega}')$ is the set of unit vectors $\hat{\Omega}$ such that $\hat{\Omega}' \cdot \hat{\Omega} = \cos\theta$.

To calculate the total ith angular flux $\psi_i(E', \boldsymbol{x}', \hat{\Omega}')$, we then must integrate over all initial energies E_0, $E' \leq E_0 \leq E'/(1-2\alpha)$ and over all λ along the ray $\boldsymbol{x}' - \lambda\hat{\Omega}'$ until λ_{max}, where $\boldsymbol{x}' - \lambda_{max}\hat{\Omega}'$ is a point on the surface of the detector:

$$\begin{aligned} \psi_i(E', \boldsymbol{x}', \hat{\Omega}') = &\int_0^{\lambda_{max}} d\lambda \frac{n}{4\pi\lambda^2} \int_{E'}^{E'/(1-2\alpha)} dE_0 \\ &\times \frac{d\sigma(E_r, E_0)}{dE_r} \int_{\mathcal{U}(\hat{\Omega}')} d\Omega_0 \psi_{i-1}(E_0, \boldsymbol{x}_0, \hat{\Omega}_0) \end{aligned} \tag{D13}$$

The interaction rates follow from the ψ_i immediately:

$$R_i(E_r') = \frac{1}{m_{Si} V} \int_V d\boldsymbol{x}' \int dE_n' \int_{4\pi} d\Omega' \psi_i(E_n', \boldsymbol{x}', \hat{\Omega}') \frac{d\sigma(E_r', E_n')}{dE_r'} \tag{D14}$$

[1] J. Hakenmüller, C. Buck, K. Fülber, G. Heusser, T. Klages, M. Lindner, A. Lücke, W. Maneschg, M. Reginatto, T. Rink, T. Schierhuber, D. Solasse, H. Strecker, R. Wink, M. Zbořil, and A. Zimbal, The European Physical Journal C **79**, 699 (2019).

[2] G. Agnolet, W. Baker, D. Barker, R. Beck, T. Carroll, J. Cesar, P. Cushman, J. Dent, S. De Rijck, B. Dutta, W. Flanagan, M. Fritts, Y. Gao, H. Harris, C. Hays, V. Iyer, A. Jastram, F. Kadribasic, A. Kennedy, A. Kubik, K. Lang, R. Mahapatra, V. Mandic, C. Marianno, R. Martin, N. Mast, S. McDeavitt, N. Mirabolfathi, B. Mohanty, K. Nakajima, J. Newhouse, J. Newstead, I. Ogawa, D. Phan, M. Proga, A. Rajput, A. Roberts, G. Rogachev, R. Salazar, J. Sander, K. Senapati, M. Shimada, B. Soubasis, L. Strigari, Y. Tamagawa, W. Teizer, J. Vermaak, A. Villano, J. Walker, B. Webb, Z. Wetzel, and S. Yadavalli (MINER Collaboration), Nuclear Instruments and Methods in Physics Research Section A: Accelerators, Spectrometers, Detectors and Associated Equipment **853**, 53 (2017).

[3] A. Leder, A. Anderson, J. Billard, E. Figueroa-Feliciano, J. Formaggio, C. Hasselkus, E. Newman, K. Palladino, M. Phuthi, L. Winslow, and L. Zhang, Journal of Instrumentation **13**, P02004 (2018).

[4] A. Aguilar-Arevalo, X. Bertou, C. Bonifazi, G. Cancelo, A. Castañeda, B. Cervantes Vergara, C. Chavez, J. C. D'Olivo, J. a. C. dos Anjos, J. Estrada, A. R. Fernandes Neto, G. Fernandez Moroni, A. Foguel, R. Ford, J. Gonzalez Cuevas, P. Hernández, S. Hernandez, F. Izraelevitch, A. R. Kavner, B. Kilminster, K. Kuk, H. P. Lima, M. Makler, J. Molina, P. Mota, I. Nasteva, E. E. Paolini, C. Romero, Y. Sarkis, M. Sofo Haro, I. a. M. S. Souza, J. Tiffenberg, and S. Wagner (CONNIE Collaboration), Phys. Rev. D **100**, 092005 (2019).

[5] R. Agnese, A. Anderson, T. Aramaki, I. Arnquist, W. Baker, D. Barker, R. B. Thakur, D. Bauer, A. Borgland, M. Bowles, P. Brink, R. Bunker, B. Cabrera, D. Caldwell, R. Calkins, C. Cartaro, D. Cerdeño, H. Chagani, Y. Chen, J. Cooley, B. Cornell, P. Cushman, M. Daal, P. D. Stefano, T. Doughty, L. Esteban, S. Fallows, E. Figueroa-Feliciano, M. Fritts, G. Gerbier, M. Ghaith, G. Godfrey, S. Golwala, J. Hall, H. Harris, T. Hofer, D. Holmgren, Z. Hong, E. Hoppe, L. Hsu, M. Huber, V. Iyer, D. Jardin, A. Jastram, M. Kelsey, A. Kennedy, A. Kubik, N. Kurinsky, A. Leder, B. Loer, E. L. Asamar, P. Lukens, R. Mahapatra, V. Mandic, N. Mast, N. Mirabolfathi, R. Moffatt, J. M. Mendoza, J. Orrell, S. Oser, K. Page, W. Page, R. Partridge, M. Pepin, A. Phipps, S. Poudel, M. Pyle, H. Qiu, W. Rau, P. Redl, A. Reisetter, A. Roberts, A. Robinson, H. Rogers, T. Saab, B. Sadoulet, J. Sander, K. Schneck, R. Schnee, B. Serfass, D. Speller, M. Stein, J. Street, H. Tanaka, D. Toback, R. Underwood, A. Villano, B. von Krosigk, B. Welliver, J. Wilson, D. Wright, S. Yellin, J. Yen, B. Young, X. Zhang, and X. Z. and, Physical Review D **95** (2017), 10.1103/physrevd.95.082002.

[6] R. Calkins (SuperCDMS Collaboration), J. Phys. Conf. Ser. **718**, 042009 (2016).

[7] M. Medhat and Y. Wang, Applied Radiation and Isotopes **84**, 13 (2014).

[8] J. L. Beck and K. M. Zuev, "Rare-event simulation," in *Handbook of Uncertainty Quantification* (Spring International Publishing, Switzerland, 2015).

[9] H. Kahn and A. W. Marshall, Journal of the Operations Research Society of America **1**, 263 (1953), https://doi.org/10.1287/opre.1.5.263.

[10] R. J. Allen, C. Valeriani, and P. R. ten Wolde, Journal of Physics: Condensed Matter **21**, 463102 (2009).

[11] J. Blanchet and H. Lam, Surveys in Operations Research and Management Science **17**, 38 (2012).

[12] S. Juneja and P. Shahabuddin, in *Simulation*, Handbooks in Operations Research and Management Science, Vol. 13, edited by S. G. Henderson and B. L. Nelson (Elsevier, 2006) pp. 291–350.

[13] R. Agnese, A. J. Anderson, T. Aramaki, I. Arnquist, W. Baker, D. Barker, R. Basu Thakur, D. A. Bauer, A. Borgland, M. A. Bowles, P. L. Brink, R. Bunker, B. Cabrera, D. O. Caldwell, R. Calkins, C. Cartaro, D. G. Cerdeño, H. Chagani, Y. Chen, J. Cooley, B. Cornell, P. Cushman, M. Daal, P. C. F. Di Stefano, T. Doughty, L. Esteban, S. Fallows, E. Figueroa-Feliciano, M. Fritts, G. Gerbier, M. Ghaith, G. L. Godfrey, S. R. Golwala, J. Hall, H. R. Harris, T. Hofer, D. Holmgren, Z. Hong, E. Hoppe, L. Hsu, M. E. Huber, V. Iyer, D. Jardin, A. Jastram, M. H. Kelsey, A. Kennedy, A. Kubik, N. A. Kurinsky, A. Leder, B. Loer, E. Lopez Asamar, P. Lukens, R. Mahapatra, V. Mandic, N. Mast, N. Mirabolfathi, R. A. Moffatt, J. D. Morales Mendoza, J. L. Orrell, S. M. Oser, K. Page, W. A. Page, R. Partridge, M. Pepin, A. Phipps, S. Poudel, M. Pyle, H. Qiu, W. Rau, P. Redl, A. Reisetter, A. Roberts, A. E. Robinson, H. E. Rogers, T. Saab, B. Sadoulet, J. Sander, K. Schneck, R. W. Schnee, B. Serfass, D. Speller, M. Stein, J. Street, H. A. Tanaka, D. Toback, R. Underwood, A. N. Villano, B. von Krosigk, B. Welliver, J. S. Wilson, D. H. Wright, S. Yellin, J. J. Yen, B. A. Young, X. Zhang, and X. Zhao (SuperCDMS Collaboration), Phys. Rev. D **95**, 082002 (2017).

[14] D. Brown, M. Chadwick, R. Capote, A. Kahler, A. Trkov, M. Herman, A. Sonzogni, Y. Danon, A. Carlson, M. Dunn, D. Smith, G. Hale, G. Arbanas, R. Arcilla, C. Bates, B. Beck, B. Becker, F. Brown, R. Casperson, J. Conlin, D. Cullen, M.-A. Descalle, R. Firestone, T. Gaines, K. Guber, A. Hawari, J. Holmes, T. Johnson, T. Kawano, B. Kiedrowski, A. Koning, S. Kopecky, L. Leal, J. Lestone, C. Lubitz, J. Márquez Damián, C. Mattoon, E. McCutchan, S. Mughabghab, P. Navratil, D. Neudecker, G. Nobre, G. Noguere, M. Paris, M. Pigni, A. Plompen, B. Pritychenko, V. Pronyaev, D. Roubtsov, D. Rochman, P. Romano, P. Schillebeeckx, S. Simakov, M. Sin, I. Sirakov, B. Sleaford, V. Sobes, E. Soukhovitskii, I. Stetcu, P. Talou, I. Thompson, S. van der Marck, L. Welser-Sherrill, D. Wiarda, M. White, J. Wormald, R. Wright, M. Zerkle, G. Žerovnik, and Y. Zhu, Nuclear Data Sheets **148**, 1 (2018), special Issue on Nuclear Reaction Data.

[15] N. Mast, A. Kennedy, H. Chagani, D. Codoluto, M. Fritts, R. Harris, A. Jastram, R. Mahapatra, V. Mandic, N. Mirabolfathi, M. Platt, and D. Strandberg, Nuclear Instruments and Methods in Physics Research Section A: Accelerators, Spectrometers, Detectors and Associated Equipment **904**, 15 (2018).

[16] N.B. It was found that the precise angular and spatial distribution of neutrons at the surface of the detector did not significantly affect the results. In particular, a homogeneous flux inside the detector and isotropic emission from a 10 cm sphere surrounding the detector were both tested, with no significant changes from the method described in the text.